Inductive Power Transfer System With Maximum Efficiency Tracking Control and Real-Time Mutual Inductance Estimation

Fei Xu, *Student Member, IEEE*, Siu-Chung Wong, *Senior Member, IEEE*, and Chi K. Tse, *Fellow, IEEE*

***Abstract*—To design simple and efficient inductive power transfer (IPT) systems, a minimum number of conversion stages and an effective maximum efficiency tracking (MET) are the primary design criteria. The MET control uses a fast mutual inductance estimation (MIE) algorithm to achieve fast tracking of the maximum efficiency point, especially when the variation of the gap distance and misalignment of the magnetic coupler are significant. The feedback control of the MET-MIE IPT system should be designed without a wireless communication channel to improve stability and robustness. In this article, a novel MET-MIE control strategy is proposed for achieving simplicity and high efficiency in IPT systems. Verifications are provided by simulations and experiments. It is shown that maximum efficiency can be tracked with less than 4% error in MIE under significant variation of the gap distance and misalignment of the magnetic coupler.**

***Index Terms*—Inductive-power-transfer (IPT), maximum efficiency tracking (MET), misalignment, mutual inductive estimation.**

I. Introduction

THE development of wireless power transfer (WPT) technology has progressed rapidly in the past three decades and has now reached the stage of commercialization [1]. The inductive power transfer (IPT), in particular, is a near field WPT technology transferring power in a short distance by inductive coupling via magnetic fields with relatively high efficiency [2]. The IPT technology is now widely used in consumer electronics [3], biomedical implants [4], metro rail transit [5], and electric vehicles (EV) [6], [7].

The simplest IPT topology is shown in Fig. 1(a). It consists of a power source V_{in}, an inverter, a magnetic coupler, a rectifier, and load R_L. Among the basic compensation schemes, namely, series–parallel (S–P), parallel–parallel (P–P), parallel–series (P–S), and series–series (S–S) compensation schemes, the S–S scheme is most widely used for its low sensitivity to variations of load and mutual inductance [8]. Unfortunately, being a resonant converter system, the maximum efficiency of this simple IPT system can only be achieved if the following conditions are satisfied [6], [8]: 1) load R_L equals a matched load R_m, which varies with mutual inductance M, and 2) the phase difference between the inverter voltage and current must be slightly positive in order to permit zero-voltage switching (ZVS) of all the MOSFET power switches. To cater for a wider load range, an extra dc/dc converter responsible for transforming R_L dynamically into R_m as seen by the rectifier has been proposed using a

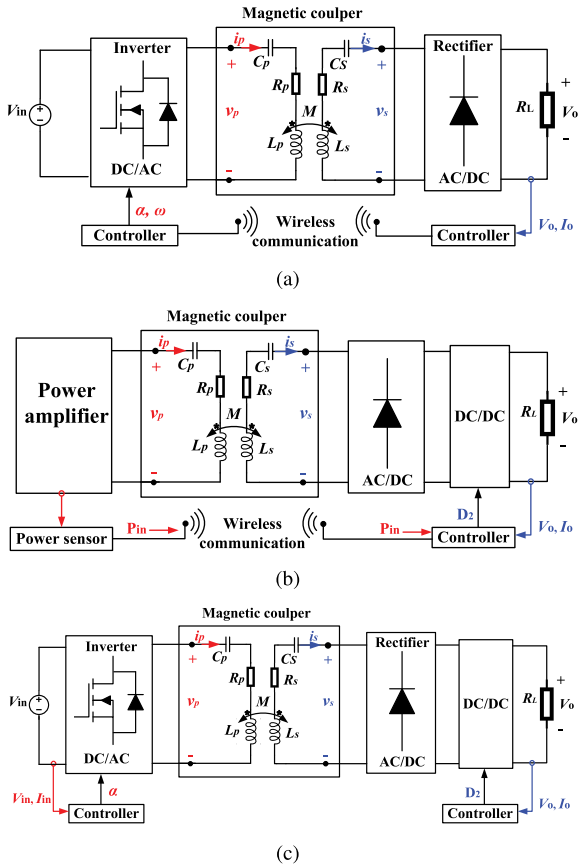

Fig. 1. (a) Simplest S-S compensated IPT system; (b) with extra DC/DC converter at load side [9], [10]; (c) with extra DC/DC converter at load side but without fast wireless communication channel [11].

Manuscript received May 8, 2021; revised July 30, 2021 and October 6, 2021; accepted October 31, 2021. Date of publication November 10, 2021; date of current version January 19, 2022. This work was supported by Hong Kong RGC Theme-based Research Scheme under Grant T23-701/20-R. Recommended for publication by Associate Editor T. Mishima. *(Corresponding author: Fei Xu.)*

Fei Xu and Siu-Chung Wong are with the Department of Electronic and Information Engineering, The Hong Kong Polytechnic University, Kowloon, Hong Kong (e-mail: feifly.xu@connect.polyu.hk; enscwong@polyu.edu.hk).

Chi K. Tse is with the Department of Electrical Engineering, City University of Hong Kong, Kowloon, Hong Kong (e-mail: cktse@ieee.org).

Color versions of one or more figures in this article are available at https://doi.org/10.1109/TPEL.2021.3126884.

Digital Object Identifier 10.1109/TPEL.2021.3126884

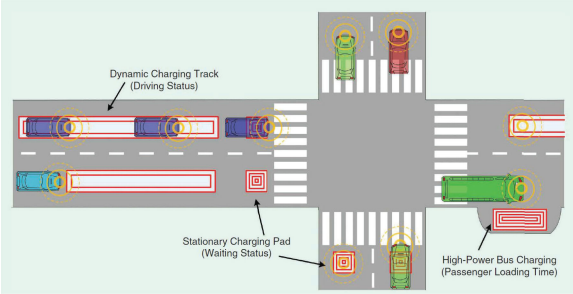

Fig. 2. Dynamic and static charging scenario of a EV driving on a road [7].

power amplifier as power source, as shown in Fig. 1(b) [9], [10]. However, the efficiency gained from impedance matching may not compensate for the extra losses due to the presence of more power conversion stages in the low-efficiency power amplifier and the cascaded buck–boost dc/dc converter. Moreover, the system efficiency can be maximized using the information of input power and output power, but it necessitates the use of wireless communication. In order to achieve high efficiency over a wider load range with output regulation, and to eliminate the need for wireless communication, an extra dc/dc converter responsible for output regulation and an independent maximum efficiency tracking (MET) control implemented in the inverter are proposed for the simple IPT system shown in Fig. 1(c) [11]. It should be noted that the MET control require information of R_L and M. The inverter is controlled by modulating a phase angle α, corresponding to the duty cycle of the inverter (described in Section II), and the process is digitally controlled by an inherently slow perturbation and observation (P&O) algorithm, which aims to minimize the input current and the input power of the inverter. The drawbacks of this system are that 1) the extra dc/dc converter stage incurs extra loss, 2) ZVS cannot be achieved for all power switches, and 3) the P&O control is inherently slow due to the random perturbation speed and amplitude to search the optimal control variable when the load or mutual inductance have variations.

To alleviate the above problems, the duty cycle regulated extra dc/dc converter can be replaced by an active rectifier with appropriate control to achieve the required impedance matching and output regulation with ZVS in all power switches [12]–[14]. Unfortunately, the mutual inductance M is not measured dynamically and its value is a design parameter for achieving a specific converter voltage ratio [12]. Moreover, M is also a reference parameter for efficiency optimization [13] and is used for the determination of control parameters [14]. Thus, M is an important design parameter for the accurate control of an IPT system in dynamic scenarios [12]–[14], where the misalignment and gap distance between the transmitting coil and receiving coil may change with time. For example, when a EV is driving on the road, the gap distances are varying with time [7], especially under different load conditions as shown in Fig. 2. The accuracy of the control can be greatly compromised without real-time measurement of M [12]–[14]. In a recent work [15], the mutual inductance M is dynamically measured for facilitating real-time control against misalignment and variation of the gap distance of the magnetic coupler. However, the system configuration is still inadequate in the following aspects: 1) it requires a primary side dc/dc converter for the regulation of the output voltage, thus incurring extra loss; 2) the impedance matching is performed by a secondary T-type filter built with a matrix of relay switches that is too slow to keep up with the speed of impedance matching. Moreover, The control relies on a high-speed wireless data link for the exchange of important control information from one switching cycle to another between the primary and the secondary controllers.

Many attempts have been made to perform real-time measurement (or estimation) of M. By measuring the zero crossing time instants of the square inverter voltage, the voltage of the parallel compensation capacitor and the current of the transmitter of the magnetic coupler of an *LCC–LCC* compensated IPT converter system, M can be estimated from the time lapse between successive zero-crossing time instants [16]. While, the calculation is subject to high round–up (or round–down) errors when the resolution of the data point acquired is not sufficiently fine. In [17], M is estimated by operating at a test frequency different from the normal resonant frequency. The input impedance derived has a singularity at the resonant frequency that makes this method unsuitable for real-time measurement at resonance. In a recent work [18], extra bidirectional switch and capacitor are added in parallel to the primary side compensation capacitor of an S–S compensated IPT system. The S–S IPT system operates as usual when the switch is OFF. The switch is turned ON when the information of M is needed. The information of M can be estimated from the real-time measurements of the dc input voltage and the two-set values of the rms current of the transmitter and operating frequency during tuned and detuned operations. However, the additional bidirectional switch needs two extra MOSFETs, which may incur loss and increase the cost and complexity of the system. In another recent work [19], a method of shorting the secondary active rectifier to ground for a brief duration is proposed to estimate M for the S–S compensation IPT system by precisely detecting the phase differences between the switching signal of the inverter and the transmitter current of the magnetic coupler. In addition, a topology with two sets of square wave generators having different voltage and frequency have been used [20]. The generator sets are connected with the secondary windings in series, so as to create a beat frequency out of the sum of two power signals with two frequencies and magnitudes, to drive the magnetic coupler of an S–S compensated IPT system. When the information of M is needed, the power switch is turned OFF to create a modulation of current at the receiver of the magnetic coupler. The modulated amplitude of the current at steady-state is measured to estimate M.

Some methods have been proposed to activate a measurement circuit in demand and wait until a new steady-state is reached for the actual measurement [17]–[20]. After the measurement, the measurement circuit is disabled and the converter system resumes its normal operation. The switching between two modes

TABLE I
FEATURES OF IPT SYSTEM WITH MET CONTROL AND REAL-TIME MIE

Feature	[10], [11]	[12]	[13]–[15]	[16]	[17]–[20]	[21]	proposed
Simplest topology with active rectifier	×	×	√	×	×	√	√
ZVS for all MOSFETs	–	×	√	×	×	×	√
Fast MET with real-time estimation of M	×	×	×	√	×	×	√
Specific and simple M estimation	×	×	×	√	×	×	√
General but complicated M estimation	×	×	×	×	√	√	×
Wireless communication for feedback control not necessary	×	√	×	×	√	√	√

Keys: (check, Yes), (–, Unknown), (×, No).

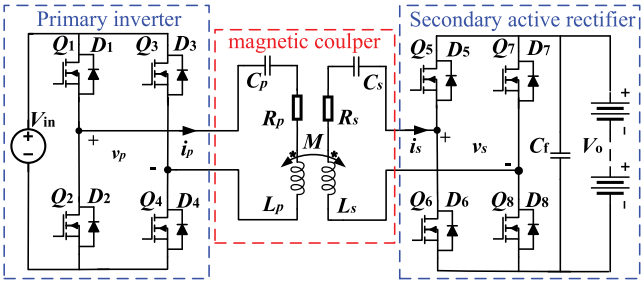

Fig. 3. Simplest S–S compensation IPT topology with active rectifier.

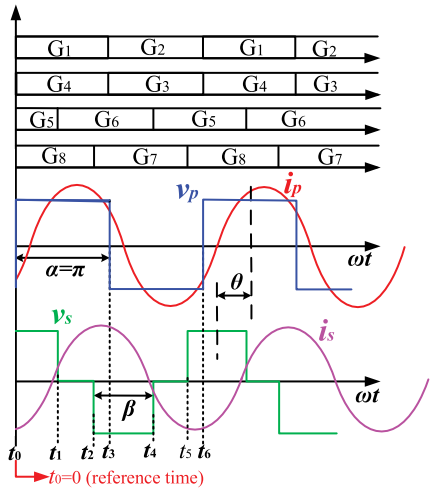

Fig. 4. Steady-state operating waveforms.

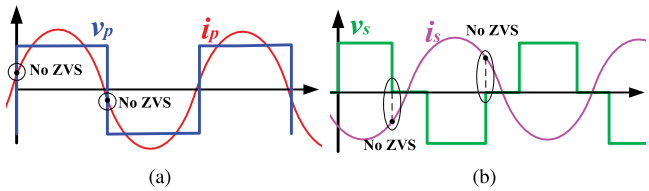

Fig. 5. Steady-state waveforms corresponding to absence of ZVS. (a) Primary side. (b) Secondary side.

of operation can complicate the control, disrupt the normal operation of the system, and decrease the controller speed and the overall system performance.

The desirable features of the MET control implemented in an S–S compensation IPT system are shown in Table I. Compared with the existing methods, the merits of our proposed method include 1) using simplest topology with an active rectifier, 2) achieving ZVS for all MOSFETs, 3) implementing MET control with real-time estimation of mutual inductance for dynamic scenarios, and 4) requiring no wireless communication between the primary and secondary sides.

II. SYSTEM STRUCTURE AND STEADY-STATE MODEL

Fig. 3 shows a simplest S–S compensation IPT system with a secondary active rectifier and battery load. For ease of reference, subscripts p and s denote parameters in the primary and secondary sides, respectively. The magnetic coupler has self-inductances L_p with resistance R_p and L_s with resistance R_s, and mutual inductance M. The series–series compensation capacitors C_p and C_s are driven by the primary inverter with a high frequency voltage v_p and the secondary active rectifier with a high frequency voltage v_s.

Power switches Q_1 to Q_8 are driven by control signals G_1 to G_8. Typical steady-state operating waveforms v_p, v_s, i_p, and i_s are shown in Fig. 4, corresponding to a power flowing from primary side to secondary side. For the primary side, transistor pairs (Q_1, Q_4) and (Q_2, Q_3) turn ON and OFF simultaneously with 50% duty cycle, which defines two levels of v_p with 50% duration of positive and negative voltages in one period. Moreover, the conduction angle $\beta \in [0, \pi]$ defines the duration of positive and negative voltages of v_s within one period. The relative phase angle $\theta \in [0, \pi/2]$ of v_p and v_s can be controlled by the relative phase of transistor pairs (Q_1, Q_2) and (Q_5, Q_6).

The time sequence $\{t_0, \ldots, t_6\}$ is the turn-ON times of one of the eight power switches within a switching period. It should be noted that the phases of i_p, i_s, v_p, and i_s shown in Fig. 4 are designed for ensuring ZVS of all transistors for the desired power flow. By changing the time sequences of control signals G_1 to G_8, a situation may arise where the phases between currents and voltages in both sides do not permit ZVS to be achieved for all switches, as shown in Fig. 5. The detailed analysis of the ZVS conditions is given in Section III-A. The initial time point $t_0 = 0$ is set as the time reference point of the time-domain model.

In general, C_p and C_s are designed to compensate L_p and L_s for matching the required resonant frequency ω in order to minimize the apparent power rating and maximize the transfer capability. The operating switching frequency is usually designed at the resonate frequency, i.e.,

$$\omega = \frac{1}{\sqrt{L_p C_p}} = \frac{1}{\sqrt{L_s C_s}}. \tag{1}$$

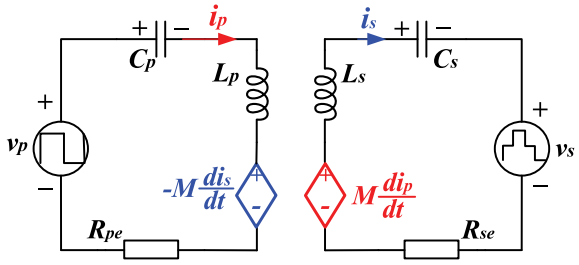

Fig. 6. Equivalent circuit of the magnetic coupler of Fig. 3.

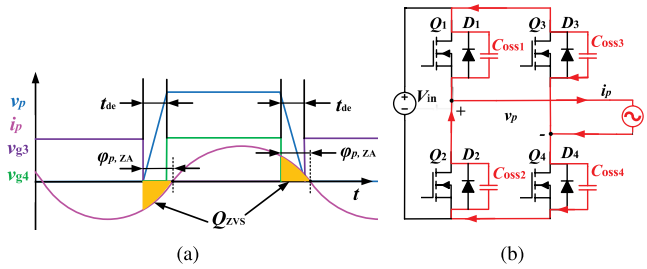

Fig. 7. Principles of ZVS soft switching about Q_4. (a) Operating waveforms. (b) Equivalent circuit during dead time.

With $t_0 = 0$, the fundamental component of $v_p(t)$ and $v_s(t)$ can be written as

$$v_p(t) = \frac{4V_{\text{in}}}{\pi}\cos\left(\omega t - \frac{\pi}{2}\right), \text{ and} \tag{2}$$

$$v_s(t) = \frac{4V_o}{\pi}\cos\left(\omega t - \frac{\pi}{2} + \theta\right)\sin\left(\frac{\beta}{2}\right). \tag{3}$$

Referring to Fig. 6 and applying KVL, we obtain

$$i_p(t)R_{pe} + L_p\frac{di_p(t)}{dt} + v_{C_p}(t) - M\frac{di_s(t)}{dt} = v_p(t) \tag{4}$$

$$i_s(t)R_{se} + L_s\frac{di_s(t)}{dt} + v_{C_s}(t) - M\frac{di_p(t)}{dt} = -v_s(t). \tag{5}$$

where $R_{pe} = R_p + 2R_{ds} + R_{C_p}$ and $R_{se} = R_s + 2R_{ds} + R_{C_s}$ are equivalent resistances of the magnetic coupler, with R_{ds} being the ON-state resistance of the MOSFET and R_{C_s} the series resistance of the capacitor. At resonance, the sum of the voltages across C_p and L_p is zero, and likewise for C_s and L_s. Thus, (4) and (5) can be approximated as

$$i_p(t) = \frac{v_p(t) - M\frac{di_s(t)}{dt}}{R_{pe}} \tag{6}$$

$$i_s(t) = \frac{M\frac{di_p(t)}{dt} - v_s(t)}{R_{se}}. \tag{7}$$

Substituting $v_p(t)$ in (2) and $v_s(t)$ in (3) into (6) and (7), and using $\omega M \gg R_{se}$ and $\omega^2 M^2 \gg R_{pe}R_{se}$ for this high-Q circuit, we obtain

$$i_p(\vartheta) = \frac{4V_o}{\pi}\frac{\sin(\frac{\beta}{2})\sin(\vartheta - \frac{\pi}{2} + \theta)}{\omega M}, \text{ and} \tag{8}$$

$$i_s(\vartheta) = \frac{4V_{\text{in}}}{\pi}\frac{\sin(\vartheta - \frac{\pi}{2})}{\omega M} \tag{9}$$

where $\vartheta = \omega t$. The transmission power for this approximated lossless system can be expressed as

$$P = \frac{1}{2\pi}\int_0^{2\pi} v_p(\vartheta)i_p(\vartheta)d\vartheta \tag{10}$$

Substituting (8) and (2) into (10), we get

$$P = \frac{8V_{\text{in}}V_o}{\pi^2\omega M}\sin\left(\frac{\beta}{2}\right)\sin(\theta). \tag{11}$$

The output power is proportional to P and can be controlled monotonically by the control angles $\beta \in [0, \pi]$, and $\theta \in [0, \pi/2]$.

III. Maximum Efficiency and Mutual Inductance Tracking

In this section, we will formulate the condition for ZVS of all power switches to minimize switching loss. With ZVS guaranteed, the conduction loss formulated in Section III-B will be minimized by finding the optimal control angles (β, θ) and the real-time estimated mutual inductance M described in Section III-D.

A. ZVS Conditions

In order to achieve ZVS, taking the primary side switch Q_4 as an example, the phase angle of current i_p should lag v_p to discharge the parasitic output capacitance C_{oss4} of Q_4 during the dead time t_{de}, as shown in Fig. 7(a), where the integral of i_p during t_{de} is denoted as Q_{ZVS}. Then, ZVS of Q_4 can be achieved when Q_{ZVS} is sufficient to charge C_{oss3} from 0 V to V_{in} and discharge C_{oss4} from V_{in} to 0 V, i.e.,

$$Q_{\text{ZVS}} = \int_0^{t_{\text{de}}} i_p dt \geq \int_0^{V_{\text{in}}} (C_{\text{oss3}} + C_{\text{oss4}})dv. \tag{12}$$

Taking the primary inverter as an example, to determine the minimum phase difference $\delta_{p,\min}$ and the minimum dead time $t_{p,\text{de}-\min}$ required by ZVS, the waveform of i_p during the dead time is expressed as a piecewise sine wave. Therefore, according to (12) and the equivalent circuit shown in Fig. 7(b), $\delta_{p,\min}$ and $t_{p,\text{de}-\min}$ can be calculated from [21], given by

$$\delta_{p,\min} = \arccos\left(1 - \frac{\sqrt{2}\pi V_{\text{in}}(C_{\text{oss3}} + C_{\text{oss4}})}{T_s I_p}\right)$$

$$\approx \sqrt{\frac{2\sqrt{2}\pi V_{\text{in}}(C_{\text{oss3}} + C_{\text{oss4}})}{T_s I_p}} \tag{13}$$

and

$$t_{\text{p,de}-\min} = \frac{\delta_{p,\min}}{2\pi}T_s \tag{14}$$

where $T_s = 2\pi/\omega$ is the switching period of the primary inverter and I_p is the root-mean-square value of i_p. Similarly, the minimum phase difference and the minimum dead time required by ZVS in secondary active rectifier can also be obtained. For simplicity, the equations are not given here. According to the design parameters listed in Table III and the data sheet value of C_{oss} of MOSFETs adopted in our experimental prototype,

TABLE II
PARAMETERS OF MAGNETIC COUPLED COILS

Parameters	Symbols	Values
Materials	Litz Wire	AWG38
Turns	n_p, n_s	30, 46
Outer Diameter	d_o_p, d_o_s	300mm, 500mm
Inner Diameter	d_{in}_p, d_{in}_s	35mm, 35 mm
Radius	r_p, r_s	0.5 mm, 0.75 mm

TABLE III
PARAMETERS OF EXPERIMENTAL PROTOTYPE

Parameters	Symbols	Values
Operating frequency	f	85 kHz
Input voltage	V_{in}	45 V
Output voltage	V_o	80 V
Rated power	P_N	120 W
Dead Time	t_{de}	300 ns
Self inductance	L_p, L_s	117.9 μH, 174.4 μH
Current Transformer	CT	TAK12-02
Digital to analog module	DA	DAC8501
Equivalent resistances	R_{pe}, R_{se}	0.27 Ω, 0.32 Ω
Compensation capacitances	C_p, C_s	29.98 nF, 20.12 nF

we arrive at a design with a margin of the minimum phase difference $\delta_{\min} = 0.14$ rad and the dead time $t_{\text{de}-\min} = 300$ ns in the primary inverter and the secondary active rectifier.

We denote by $\varphi_{p,\text{ZA}}$ and $\varphi_{s,\text{ZA}}$ the phase angle of the current lagging the voltage in primary and secondary sides, respectively. According to the steady-state operating waveforms shown in Fig. 4, $\varphi_{p,\text{ZA}} = \frac{\pi}{2} - \theta$ and $\varphi_{s,\text{ZA}} = \frac{\beta}{2} - \theta$. Then, the conditions of ZVS in both sides are

$$\frac{\pi}{2} - \theta \geq \delta_{\min}, \text{ and} \tag{15}$$

$$\frac{\beta}{2} - \theta \geq \delta_{\min}. \tag{16}$$

Since $\beta \leq \pi$, (16) implies (15). Thus, we only need to focus on (16) to guarantee ZVS of all power switches.

B. System Conduction Loss

Once ZVS is guaranteed, the system conduction losses should be dynamically optimized to achieve MET. Referring to the equivalent circuit shown in Fig. 6, the resistive power loss in the magnetic coupler can be expressed as

$$P_{\text{con-loss}} = I_p^2 R_{pe} + I_s^2 R_{se} \tag{17}$$

where I_p and I_s are the RMS values of i_p and i_s. According to (8) and (9), we have

$$I_p = \sqrt{\frac{1}{\pi}\int_0^{\pi} i_p^2(\vartheta) d(\vartheta)} = \frac{2\sqrt{2}V_o}{\pi\omega M}\sin\frac{\beta}{2}, \text{ and} \tag{18}$$

$$I_s = \sqrt{\frac{1}{\pi}\int_0^{\pi} i_s^2(\vartheta) d(\vartheta)} = \frac{2\sqrt{2}V_{\text{in}}}{\pi\omega M}. \tag{19}$$

Substituting (18) and (19) into (17), the system conduction loss $P_{\text{con-loss}}$ is given by

$$P_{\text{con-loss}}(\beta) = \frac{8V_o^2}{\pi^2\omega^2 M^2}\sin^2\frac{\beta}{2}R_{pe} + \frac{8V_{\text{in}}^2}{\pi^2\omega^2 M^2}R_{se}. \tag{20}$$

C. Optimal Solutions

In Sections III-A and III-B, the ZVS conditions and the formulation of system conduction loss are discussed. Our aim in this section is to find optimal solutions (β, θ) to modulate the inverter and active rectifier to achieve MET with ZVS given by the condition (16) and minimum conduction loss by minimizing $P_{\text{con-loss}}(\beta)$ as given in (20) at transmission power P_N given by (11). The optimization can be described as

$$\text{Minimize } \{P_{\text{con-loss}}(\beta)\} \text{ such that} \tag{21}$$

$$\begin{cases} P_N - \frac{8V_{\text{in}}V_o}{\pi^2\omega M}\sin\frac{\beta}{2}\sin\theta = 0 \\ \frac{\beta}{2} - \theta \geq \delta_{\min}. \end{cases} \tag{22}$$

This is an optimization problem with limited conditions that can be solved by using the Lagrange multiplier method. According to (21) and (22), the constrained Lagrange function can be described as

$$\begin{aligned} L(\beta, \theta, \lambda_1, \lambda_2) = {} & P_{\text{con-loss}}(\beta) \\ & + \lambda_1\left(P_N - \frac{8V_{\text{in}}V_o}{\pi^2\omega M}\sin\frac{\beta}{2}\sin\theta\right) \\ & + \lambda_2\left(\frac{\beta}{2} - \theta - \delta_{\min}\right) \end{aligned} \tag{23}$$

where, $\lambda_1 \neq 0$ and $\lambda_2 \geq 0$. The optimal solutions should satisfy the Karush–Kuhn–Tucker condition given by

$$\begin{cases} \frac{\partial L}{\partial \beta} = 0 \\ \frac{\partial L}{\partial \theta} = 0 \\ \lambda_1\left(P_N - \frac{8V_{\text{in}}V_o}{\pi^2\omega M}\sin\frac{\beta}{2}\sin\theta\right) = 0 \\ \lambda_2\left(\frac{\beta}{2} - \theta - \delta_{\min}\right) = 0. \end{cases} \tag{24}$$

Solving (24), an optimal solution of θ_{op} and β_{op} is

$$\beta_{\text{op}} = \arccos\left(1 - \frac{\pi^2\omega M P_N}{4V_{\text{in}}V_o}\right) + \delta_{\min}, \text{ and} \tag{25}$$

$$\theta_{\text{op}} = \frac{1}{2}\arccos\left(1 - \frac{\pi^2\omega M P_N}{4V_{\text{in}}V_o}\right) - \frac{1}{2}\delta_{\min}. \tag{26}$$

D. Dynamic Measurement of Mutual Inductance

In Section III-C, given a power P_N, the optimal solution $(\beta_{\text{op}}, \theta_{\text{op}})$ with maximum efficiency in an IPT system has been obtained. From (25) and (26), it is clear that the optimal solution needs the value of M. In order to realize a dynamic MET control, the mutual inductance should be estimated dynamically by a simple measurement.

According to (9), the peak value of i_s denoted as $|i_{s\_\text{peak}}|$ is given by

$$|i_{s\_\text{peak}}| = \frac{4V_{\text{in}}}{\pi\omega M}. \tag{27}$$

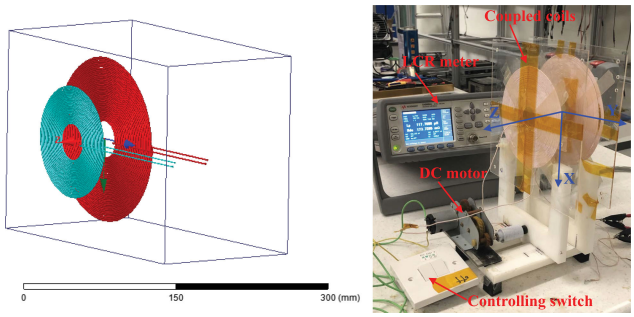

(a) (b)

Fig. 8. Magnetic coupler coils. (a) Maxwell's simulation model of magnetic coupler coils. (b) Experimental setup of the magnetic coupler coils and misalignment control.

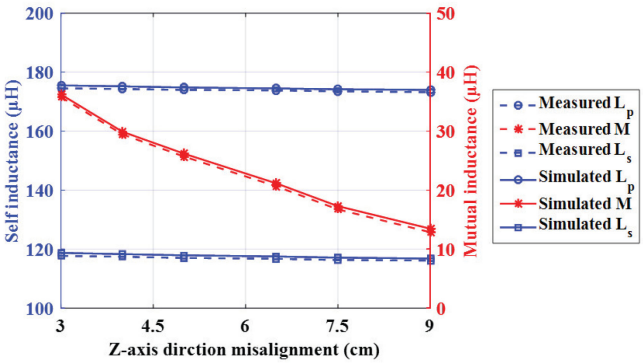

Fig. 9. Comparisons of the simulated and measured results.

It can be observed that $|i_{s\_peak}|$ is a function of the input voltage V_{in}, operating angular frequency ω and mutual inductance M. Since V_{in} and ω are known, $|i_{s\_peak}|$ can be regarded as inversely proportional to M. Therefore, we can simply measure $|i_{s\_peak}|$ to estimate M, i.e.,

$$M = \frac{4V_{in}}{\pi\omega|i_{s\_peak}|}. \tag{28}$$

IV. Design Considerations

A. Magnetic Coupler and Misalignment Measurement

A popular circular pad structure of the magnetic coupler is used in our design here, as shown in Fig. 8 with detailed parameters listed in Table II. A simulated model of the magnetic coupler is built using ANSYS Maxwell 2015 as shown in Fig. 8(a) with parameters given in Table II. A KEYSIGHT E4980AL LCR meter is used to measure the self and mutual inductances, as shown in Fig. 8(b). Fig. 9 compares the simulated and measured results of self inductances L_p, L_s and mutual inductance M. It can be observed that the measured results is nearly identical to the simulated results.

We use the origin, i.e., the distances between the primary coil and secondary coil in the *X*-axis, *Y*-axis, and *Z*-axis being zero, as a reference point. We define the position change between the primary and secondary coils in the *X*-axis/*Y*-axis direction relative to the origin as horizontal misalignment, and the change in *Z*-axis as vertical misalignment. In this article, we adopt a dc motor to modulate the position of the secondary coil in the *Z*-direction for a corresponding change of the mutual inductance, as shown in Fig. 8(b).

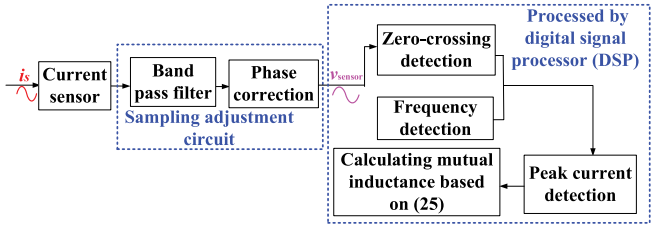

Fig. 10. Diagram of the peak current estimation.

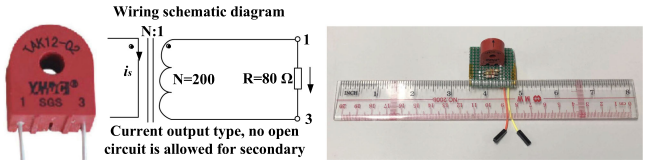

(a) (b)

Fig. 11. High-frequency pulse current sensor of TAK12-02. (a) Circuit diagram of the current sensor. (b) Photograph of the current sensor.

B. Peak Current Sampling and High Frequency Current Sensor

Using an analog-to-digital (AD) module of a digital signal processor (DSP), the sampling of current can be triggered by a flag signal in a register counter. The process of peak current detection is shown in Fig. 10. First, the secondary current i_s is sampled by a high-frequency pulse current sensor, as shown in Fig. 11. Then, the sampled signal is sent to a band-pass filter to eliminate the high frequency component and perform a phase correction. Next, the signal is sent to an ultra-fast amplifier to perform the zero-crossing detection. Finally, the zero-crossing point is taken as flag signal sending to the DSP, and after a time delay of one quarter (1/4) period, the DSP triggers the AD module to sample the current $|i_{s\_peak}|$.

The phase between the actual i_s and the measured signal $v_{sensor} = \frac{i_s R}{N}$ is important to guarantee the accuracy of the estimated mutual inductance. The circuit of the pulse current sensor with $N = 200$ and $R = 80\,\Omega$ is shown in Fig. 11(a). A comparison of waveforms of i_s and v_{sensor} at $|i_{s\_peak}| = 5$ A is shown in Fig. 12. It is clear that i_s and v_{sensor} are in phase to give the accurate calculation of M.

C. Overall Control

An overall control is shown in Fig. 13. The output voltage V_o and current I_o are sampled and then sent to the DSP. The output power P_o can be calculated through a multiplier in the DSP. A PI controller is used to regulate the output power with reference to the power P_N. Meanwhile, the secondary side peak current is sampled and the mutual inductance M can be calculated

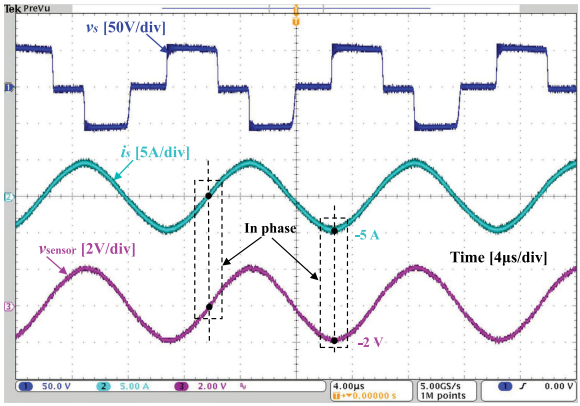

Fig. 12. Measured waveforms of i_s and v_{sensor} at $|i_{s\_\text{peak}}| = 5$ A.

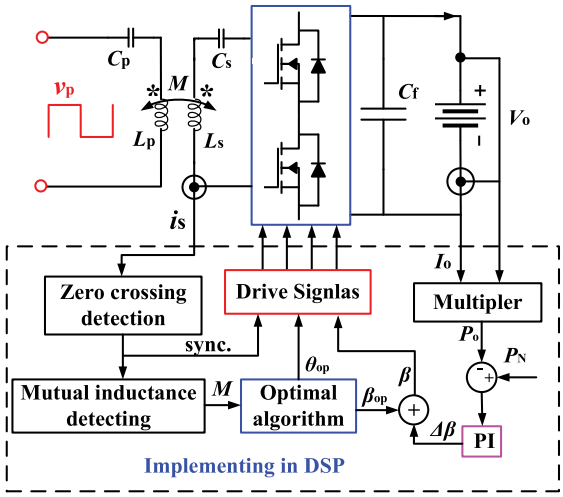

Fig. 13. Control diagram of the proposed MET with dynamic mutual inductance estimation.

according to (28). Finally, the optimal solution (β_{op}, θ_{op}) is calculated using (25) and (26) to modulate the IPT system with maximum efficiency. It should be noted that the error output of the PI controller is used to adjust $\Delta\beta$, instead of $\Delta\theta$, as shown in Fig. 13. Due to the omission of losses in (11), the error output of the PI controller will always be positive at steady state. A positive $\Delta\theta$ is more likely to violate the ZVS condition of $\frac{\beta}{2} - (\theta + \Delta\theta) \geq \delta_{\min}$, making it larger than the designed ZVS margin from which ZVS will be lost. On the contrary, a positive $\Delta\beta$ will never violate the ZVS condition.

V. Simulation and Experimental Verifications

A. Simulations

In order to verify the feasibility and accuracy of our proposed dynamic MET control strategy, simulations are carried out under MATLAB/Simulink 17.0 using the same circuit of the experimental setup. The parameters used in the simulation are shown in Table III. The switching frequency is 85 kHz and M ranges from 21.66 to 36.15 μH. Fig. 15(a) shows the transient simulated waveforms with our proposed dynamic MET

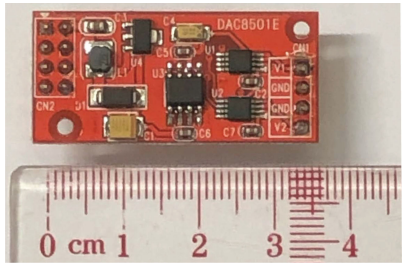

Fig. 14. Photograph of digital-to-analog module (DAC8501E).

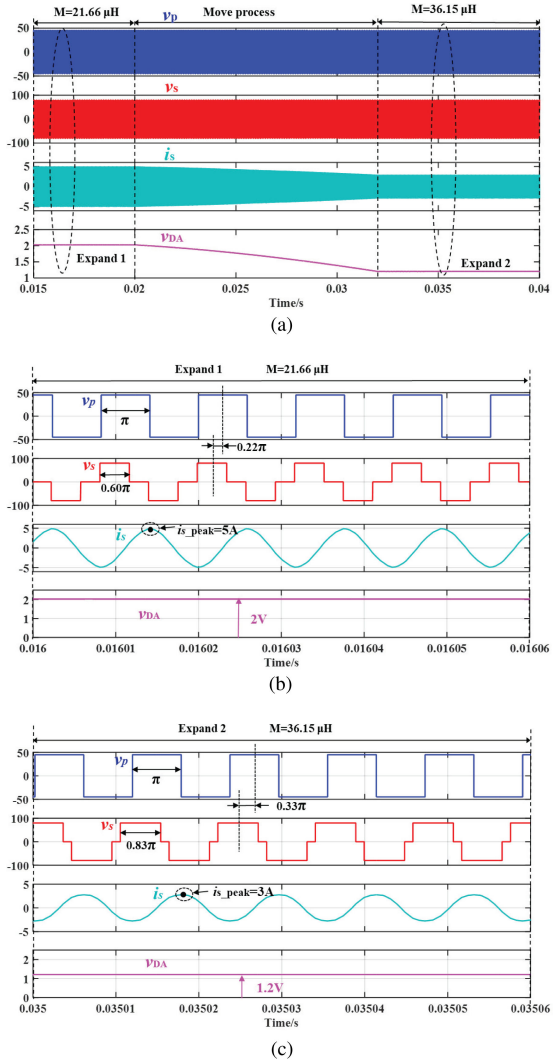

Fig. 15. Simulated waveforms under our proposed dynamic MET control. (a) Transient waveforms when M increases from 21.66 μH at 0.02 s to 36.15 μH at 0.032 s. (b) Steady-state waveforms at $M = 21.66\,\mu$H. (c) Steady-state waveforms at $M = 36.15\,\mu$H.

control strategy. The mutual inductance M increases linearly from 21.66 μH at 0.02 s to 36.15 μH at 0.032 s to imitate the mechanical moving process in experiments. Fig. 15(b) and (c) is enlarged views of the steady-state waveforms under $M = 21.66\,\mu$H and $M = 36.15\,\mu$H, respectively. Considering the conduction loss, according to (25) and (26), the

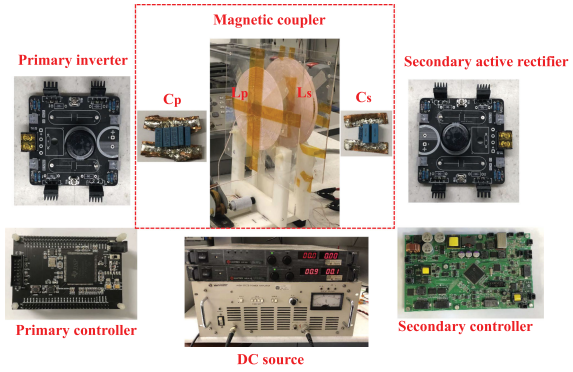

Fig. 16. Photograph of the experimental prototype.

theoretical optimal solution is $(\beta_{\text{op1}}, \theta_{\text{op1}}) = (0.58\pi, 0.23\pi)$ at $M = 21.66\,\mu$H, and $(\beta_{\text{op2}}, \theta_{\text{op2}}) = (0.82\pi, 0.33\pi)$ at $M = 36.15\,\mu$H. It can be found that the simulated θ is comparable with the theoretical value, while the simulated β is slightly larger than that of the theoretical lossless value after the feedback control is included because a slightly larger $\Delta\beta$ is needed to compensate for the system loss.

In Fig. 15, v_{DA} is the sampled peak of v_{sensor}, which tracks i_s well. In the experiments, in order to observe the estimation results directly, the estimated value of M in the DSP is converted to an analog signal by a digital-to-analog (DA) module. Here, we adopt DAC8501E as the DA module, as shown in Fig. 14.

B. Experimental Verification

An experimental prototype is built, as shown in Fig. 16, to verify the effectiveness of our proposed dynamic MET control. The parameters of the prototype are listed in Table III. Both primary and secondary sides adopt the DSP TMS320F28335 as the microcontrollers. All voltages and currents are captured by a Tektronix DPO 4104 Oscilloscope.

The experimental results are shown in Fig. 17, which have good agreements with the simulation results shown in Fig. 15, where positions A and B represent distances of 3 and 6.4 cm, respectively, in the *Z*-direction between the primary and secondary coils, which correspond to the measured mutual inductances of 36.15 and 21.66 μH, respectively.

Fig. 17(a) shows the dynamic experimental waveforms with the mutual inductance changing from 36.15 μH in position A to 21.66 μH in position B, and Fig. 17(d) shows the movements from position B to position A. Fig. 17(b) gives the steady-state waveforms in position B and Fig. 17(e) gives the steady-state waveforms in position A. It is clearly the v_{sensor} can well track the secondary peak current i_s both in dynamic and steady state and the output of DA module v_{DA} can well track the peak envelope of v_{sensor}. This verifies that our designed control strategy can well estimate the mutual inductance. Fig. 17(c) and (f) shows the steady-state waveforms of v_p, i_p, v_s and i_s at positions B and A, respectively. It can be observed that ZVS is achieved and the optimal solutions are identical to the simulated and theoretical values.

TABLE IV
COMPARISON OF OPTIMAL SOLUTIONS

Unit (rad)	Theoretical	Simulated	Experimental
β_1	0.82π	$\approx 0.83\pi$	$\approx 0.88\pi$
θ_1	0.33π	$\approx 0.33\pi$	$\approx 0.33\pi$
β_2	0.58π	$\approx 0.60\pi$	$\approx 0.63\pi$
θ_2	0.22π	$\approx 0.22\pi$	$\approx 0.22\pi$

C. Measured Results Analysis

Fig. 18 shows the estimated results of mutual inductance under six different positions. In order to improve the accuracy of the identification results, the highest and lowest point envelopes of i_s are continuously sampled, and the average value is used to solve the mutual inductance. It can be observed that the values of estimation error $\xi = |\frac{\text{Measured M} - \text{Estimated M}}{\text{Measured M}}| \times 100\%$ are all less than 4%, which show that our proposed method of estimating mutual inductance is feasible and accurate. In addition, we can observe that ξ increases slightly with increasing misalignment. This indicates that the proposed method is more accurate when the coupling of the coils is stronger. It can be observed that with an increase in M, β would also increase. Since $\beta \in [0, \pi]$, using (28) and the system parameters listed in Table III, the estimated range of M is 0–45.53 μH. However, from Fig. 18, it can be observed that with the decrease of M, the estimated error ξ would increase. Thus, to improve the estimation accuracy, e.g., $\xi < 4\%$, M should be larger than 13.46 μH.

The powers and efficiencies are measured by a precision power scope YOKOGAWA PX8000. The captured screen of the measured results of position A and position B are shown in Fig. 19. The measured maximum efficiency curve under the six positions is shown in Fig. 20. It can be observed that the maximum efficiency is 93.6% under a strong magnetic coupling at $M = 36.15\,\mu$H, while the minimum efficiency is 88.3% under a weak coupling at $M = 21.66\,\mu$H. With increasing distance between the primary and secondary coils, i.e., decreasing M, the efficiency decreases as a larger current is needed to get the same power.

A summary of the control angles used for theoretical calculation, simulation and experiment are listed in Table IV. The column under "Theoretical" are two sets of control angles calculated directly from (25) and (26) at $M = 36.15\,\mu$H and 21.66 μH, respectively. The columns under "Simulated" and "Experimental" are the corresponding control angles compensated by the control as shown in Fig. 13 at steady state. Both the theoretical calculation and simulation include the same conduction loss. The experiment includes conduction loss, switching loss, and all other losses. The control angle β becomes larger with more loss after feedback compensation is applied, as shown in Fig. 13.

A comparison of the theoretical, simulated and experimental system efficiencies for $M = 36.15\,\mu$H and 21.66 μH are listed in Table V, where the theoretical efficiency is calculated by $\eta = \frac{P_N}{P_N + P_{\text{con-loss}}}$ at the optimal control angles without feedback control. The small deviation of control angles compensated by the control loop accounts for the lower efficiency of

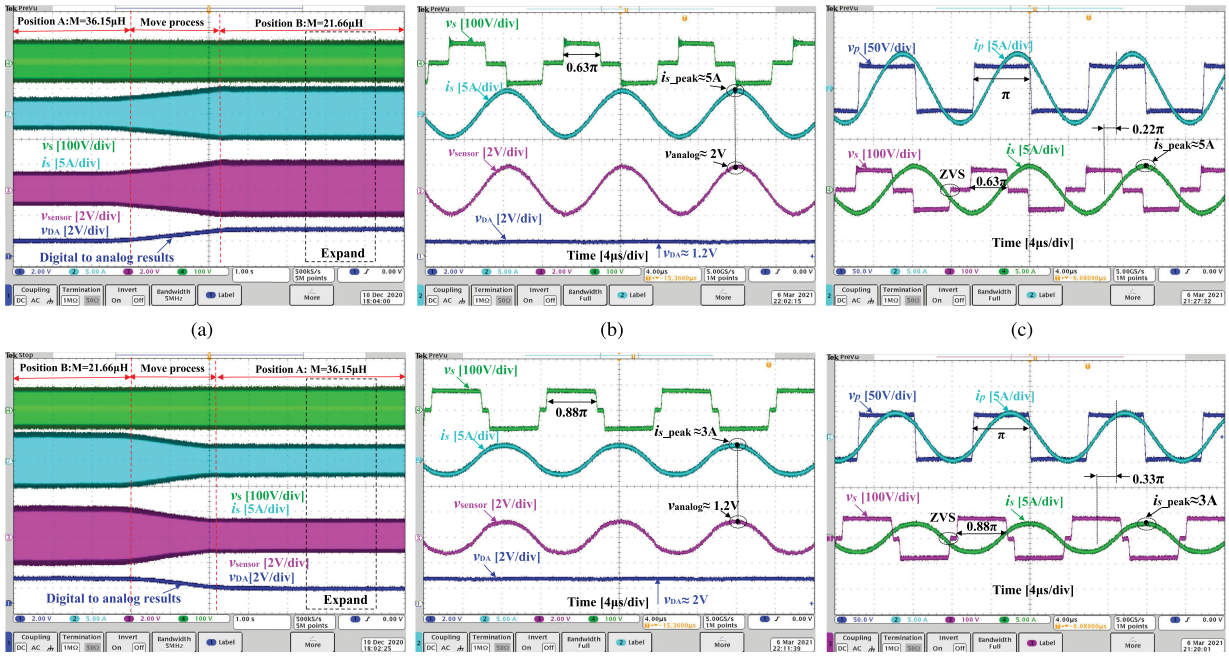

Fig. 17. Experimental waveforms under our proposed dynamic MET control. (a) Transient waveforms moving from position A to position B. (b) Steady-state waveforms at position B. (c) Corresponding steady-state waveforms of v_p, i_p, v_s and i_s at position B. (d) Transient waveforms from position B to position A. (e) Steady-state waveforms at position A. (f) Corresponding steady state waveforms of v_p, i_p, v_s and i_s at position A.

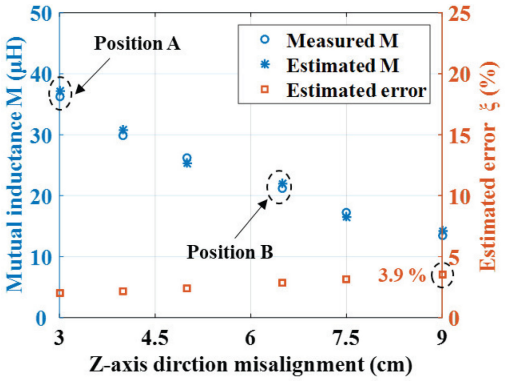

Fig. 18. Comparisons of estimating results with measured values.

Fig. 19. Screen capture of power analyzer at (a) $M = 36.15\,\mu$H and (b) $M = 21.66\,\mu$H.

TABLE V
COMPARISON OF EFFICIENCY RESULTS

Efficiency (%)	Theoretical	Simulated	Experimental
$M = 36.15\ \mu$H	96.3%	95.2%	93.6%
$M = 21.66\ \mu$H	92.1%	91.0%	88.3%

the simulated and experimental results. The reason for the differences between the theoretical and experimental efficiency data shown in Table V is that only conduction loss has been used to calculate the theoretical efficiency and the turn-OFFloss is not included. Since $\alpha = \pi$ and according to Fig. 4, we see that, on the primary side, Q_1 and Q_4 are turned OFF with current $i_p(t_0)$, and

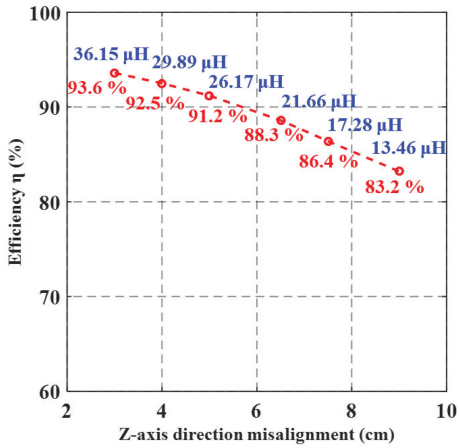

Fig. 20. Measured maximum efficiencies curve under different mutual inductances.

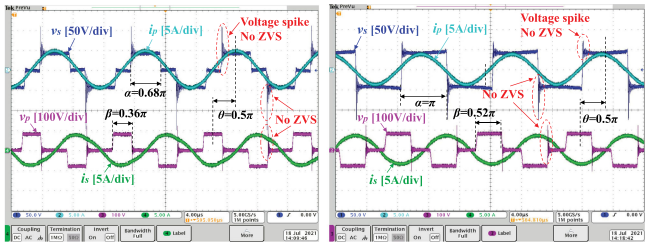

(a) (b)

Fig. 21. Experimental steady-state waveforms of v_p, i_p, v_s, and i_s under impedance matching condition under (a) $M = 21.66\,\mu$H and (b) $M = 29.89\,\mu$H.

Q_2 and Q_3 are turned OFF with current $i_p(t_3)$. Similarly, on the secondary side, Q_5 and Q_8 are turned OFF with $i_s(t_1)$ and $i_s(t_2)$, respectively, and Q_6 and Q_7 are turned OFF with $i_s(t_4)$ and $i_s(t_5)$, respectively. By symmetry, we have $|i_p(t_0)| = |i_p(t_3)|$, $|i_s(t_1)| = |i_s(t_4)|$ and $|i_s(t_2)| = |i_s(t_5)|$. The turn-OFF loss in the primary and secondary sides can be readily found [24], i.e.,

$$P_{\mathrm{sw},p} = 2 \times \frac{1}{3T} V_{\mathrm{in}} |i_p(t_0)| t_{\mathrm{off}} \tag{29}$$

$$P_{\mathrm{sw},s} = \frac{1}{3T} V_o |i_s(t_1)| t_{\mathrm{off}} + \frac{1}{3T} V_o |i_s(t_2)| t_{\mathrm{off}} \tag{30}$$

where t_{off} is the turn-OFF time of the MOSFET, which is approximately equal to the dead time t_{de}. According to the optimal theoretical angle variables β and θ listed in Table IV, the total turn-OFF losses for $M = 36.15\,\mu$H and 21.66 μH can be found as 2.9 and 5.1 W, respectively. Considering the turn-OFF losses, the theoretical efficiencies are 94.2% and 88.7%, respectively, which are close to the measured values of 93.6% and 88.3%.

D. Efficiency Comparison

The impedance matching control strategy is a popular efficiency optimization method, which can achieve a global minimum conduction loss of an IPT system [22], [23]. A comparison of our proposed optimal control strategy and the impedance matching should be considered.

Fig. 21 shows the steady-state waveforms of impedance matching for $M = 29.89\,\mu$H and 21.66 μH. It can be observed that ZVS cannot be achieved, and the high voltage spikes and oscillations would incur a large switching loss. The measured system efficiencies are 89.1% and 85.9% corresponding to $M = 29.89$ and 21.66 μH, respectively, which are both lower than the measured values of 92.5% and 89.6% using our proposed optimal control scheme shown in Fig. 20.

E. Transients With Stepping Output Voltage

With the output voltage stepped between 50 and 80 V, the waveforms of v_s, i_s I_o, V_o and power $P_o = V_o I_o$ are measured and shown in Fig. 22(a). Also, Fig. 22(b) and (c) is the corresponding steady-state waveforms for $V_o = 50$ and 80 V, respectively. It can be observed that P_o is kept constant at 120 W under step changes of V_o, verifying the stable constant power operation of the converter under stepping output voltage. In addition, it can be observed that the peak value of i_s has no variations in Fig. 22(a), which means that the mutual inductance can be estimated accurately even when the load changes.

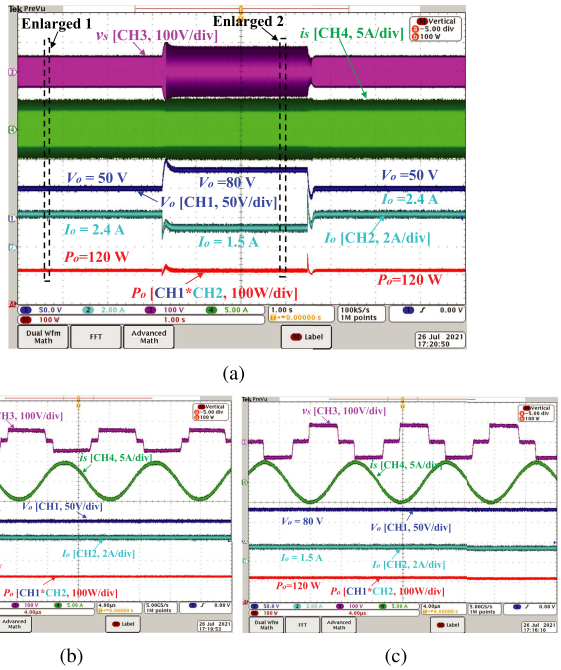

(a)

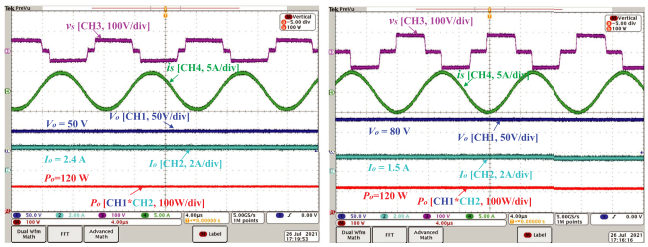

(b) (c)

Fig. 22. Experimental waveforms of the IPT system under the proposed control strategy. (a) Transient waveforms of V_o steps from 50 to 80 V and back to 50 V. (b) Steady state waveforms at $V_o = 50$ V. (c) Steady state waveforms at $V_o = 80$ V.

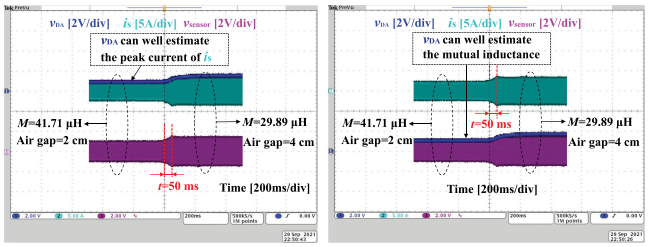

(a) (b)

Fig. 23. Experimental transient waveforms of moving from $M = 41.67\mu$H to $M = 29.89\mu$H. (a) V_{DA} can well track peak envelope of i_s. (b) V_{DA} can well track peak can well track the peak envelope of v_{sensor}.

F. Discussions on Practicability

It should be noted that the experimental platform in this article is a scale-down prototype, which is used to imitate the variations of mutual inductance M in practice. In our experiment, the receiving coil is driven by a 5 V dc motor with a small torque. Thus, the variation speed of M is slower compared with an actual EV driving on the road.

To speed up the movement of the receiving coil, a mechanical device is used, and the waveforms corresponding to a high-speed receiving coil are shown in Fig. 23. It can be observed that it takes 50 ms to drive the receiving coil to move a gap distance of 2 cm, and the average speed is $v = 2$ cm in 50 ms, i.e., 1.44 km/h.

The radius of transmitting and receiving coils are 48 and 80 mm, respectively, which are much smaller than the coils used in a real EV. Assuming the setup is a 1/15 scale-down model, the change of M is almost the same as it is at 21.6 km/h in a real-scale IPT system used in an EV. In Fig. 23, it is clear the $v_{\rm sensor}$ can well track the secondary peak current $|i_{s\_{\rm peak}}|$ in dynamic state and the output of DA module $v_{\rm DA}$ can well track the peak envelope of $v_{\rm sensor}$, verifying the ability of our control strategy in estimating the mutual inductance with the receiving side being driven at about 20 km/h over a transmitter.

In addition, the delivering power of 120 W in this article is lower than the usual charging power applied to an EV. For high-power applications, the coil size would be larger, and the actual input voltage $V_{\rm in}$ and output voltage $V_{\rm o}$ would be higher than those used in this article. According to (25) and (26), the optimal solution ($\beta_{\rm op}$, $\theta_{\rm op}$) contains parameters of $V_{\rm in}$, $V_{\rm o}$, M, P_N, ω, and $\delta_{\rm min}$. Since the input voltage $V_{\rm in}$, operating angular frequency ω and the minimum designed ZVS angle $\delta_{\rm min}$ are all constants, the optimal solution ($\beta_{\rm op}$, $\theta_{\rm op}$) only contains three variables, namely, M, $V_{\rm o}$, and P_N, which may change in practice. Also, $V_{\rm o}$ can be sampled and M can be calculated directly using our proposed control strategy. Therefore, for high-power applications with large P_N, ($\beta_{\rm op}$, $\theta_{\rm op}$) can still calculated in the secondary microcontroller to modulate the IPT system with maximum efficiency. Also, another problem is that the sampling noise is significant at a higher power level, which may affect the accuracy of the estimated M. Thus, an advanced sampling filter algorithm is needed to reduce the sampling noise, e.g., using a recursive least square filter [25].

VI. Conclusion

This article presents an effective and fast MET control with a fast mutual inductance estimation (MIE) algorithm for fast tracking of the maximum efficiency point under variation of the gap distance and misalignment of the magnetic coupler of a series–series compensated IPT (SS-IPT) system. The system contains minimum number of power conversion stages, and achieves the best system efficiency. A feedback control of the MET-MIE SS-IPT system is designed without using a wireless communication channel for improved stability and robustness. The effectiveness of the proposed MET-MIE control is validated by simulation and experimental results. It is shown that the maximum efficiency is well tracked with less than 4% error in MIE under significant variation of the gap distance and misalignment of the magnetic coupler.

References

[1] W. Zhong and S. Y. R. Hui, "Maximum energy efficiency operation of series-series resonant wireless power transfer systems using on-off keying modulation," *IEEE Trans. Power Electron.*, vol. 33, no. 4, pp. 3595–3603, Apr. 2018.

[2] S. Y. R. Hui, W. Zhong, and C. K. Lee, "A critical review of recent progress in mid-range wireless power transfer," *IEEE Trans. Power Electron.*, vol. 29, no. 9, pp. 4500–4511, Sep. 2014.

[3] S. Y. R. Hui and W. W. C. Ho, "A new generation of universal contactless battery charging platform for portable consumer electronic equipment," *IEEE Trans. Power Electron.*, vol. 20, no. 3, pp. 620–627, May 2005.

[4] Q. Chen, S. C. Wong, C. K. Tse, and X. Ruan, "Analysis, design, and control of a transcutaneous power regulator for artificial hearts," *IEEE Trans. Biomed. Circuit Syst.*, vol. 3, no. 1, pp. 23–31, Feb. 2009.

[5] J. H. Kim *et al.*, "Development of 1-MW inductive power transfer system for a high-speed train," *IEEE Trans. Ind. Electron.*, vol. 62, no. 10, pp. 6242–6250, Oct. 2015.

[6] Z. Huang, S. C. Wong, and C. K. Tse, "Design of a single-stage inductive power-transfer converter for efficient EV battery charging," *IEEE Trans. Veh. Tech.*, vol. 66, no. 7, pp. 5808–5821, Jul. 2017

[7] H. Zhang, F. Lu and C. Mi, "An electric roadway system leveraging dynamic capacitive wireless charging: Furthering the continuous charging of electric vehicles," *IEEE Electrific. Mag.*, vol. 8, no. 2, pp. 52–60, Jun. 2020.

[8] W. Zhang, S. C. Wong, C. K. Tse, and Q. Chen, "Design for efficiency optimization and voltage controllability of series-series compensated inductive power transfer systems," *IEEE Trans. Power Electron.*, vol. 29, no. 1, pp. 191–200, Jan. 2014.

[9] M. Fu, C. Ma, and X. Zhu, "A cascaded boost-buck converter for high efficiency wireless power transfer systems," *IEEE Trans. Ind. Informat.*, vol. 10, no. 3, pp. 1972–1980, May 2014.

[10] M. Fu, H. Yin, X. Zhu, and C. Ma, "Analysis and tracking of optimal load in wireless power transfer systems," *IEEE Trans. Power Electron.*, vol. 30, no. 7, pp. 3952–3963, Jul. 2015.

[11] W. X. Zhong and S. Y. R. Hui, "Maximum energy efficiency tracking for wireless power transfer systems," *IEEE Trans. Power Electron.*, vol. 30, no. 7, pp. 4025–4034, Jul. 2015.

[12] R. Mai, Y. Liu, Y. Li, P. Yue, G. Cao, and Z. He, "An active-rectifier-based maximum efficiency tracking method using an additional measurement coil for wireless power transfer," *IEEE Trans. Power Electron.*, vol. 33, no. 1, pp. 716–728, Jan. 2018.

[13] Z. Huang, S. Wong, and C. K. Tse, "An inductive-power-transfer converter with high efficiency throughout battery-charging process," *IEEE Trans. Power Electron.*, vol. 34, no. 10, pp. 10245–10255, Oct. 2019.

[14] Y. Jiang, L. Wang, J. Fang, C. Zhao, K. Wang, and Y. Wang, "A joint control with variable ZVS angles for dynamic efficiency optimization in wireless power transfer system," *IEEE Trans. Power Electron.*, vol. 35, no. 10, pp. 11064–11081, Oct. 2020.

[15] Y. Liu and H. Feng, "Maximum efficiency tracking control method for WPT system based on dynamic coupling coefficient identification and impedance matching network," *IEEE J. Emerg. Sel. Topics Power Electron*., vol. 8, no. 4, pp. 3633–3643, Dec. 2020.

[16] Y. W. Zhang, Y. J. Guo, Q. W. Zhu, and L. F. Wang, "Load and mutual inductance estimation based on phase-differences for electric vehicle wireless charging system," *IET Power Electron.*, vol. 12, no. 9, pp. 2345–2352, Jun. 2019.

[17] J. Yin, D. Lin, T. Parisini, and S. Y. R. Hui, "Front-end monitoring of the mutual inductance and load resistance in a series-series compensated wireless power transfer system," *IEEE Trans. Power Electron.*, vol. 31, no. 10, pp. 7339–7352, Oct. 2016.

[18] Y. G. Su, H. Y. Zhang, Z. H. Wang, A. Patrick Hu, L. Chen, and Y. Sun, "Steady-state load identification method of inductive power transfer system based on switching capacitors," *IEEE Trans. Power Electron.*, vol. 30, no. 11, pp. 6349–6355, Nov. 2015.

[19] Y. Yang, S. C. Tan, and S. Y. R. Hui, "Fast hardware approach to determining mutual coupling of series-series-compensated wireless power transfer systems with active rectifiers," *IEEE Trans. Power Electron.*, vol. 35, no. 10, pp. 11026–11038, Oct. 2020.

[20] X. Sheng and L. Shi, "Mutual inductance and load identification method for inductively coupled power transfer system based on auxiliary inverter," *IEEE Trans. Veh. Technol.*, vol. 69, no. 2, pp. 1533–1541, Feb. 2020.

[21] H. Li, J. Fang, S. Chen, K. Wang, and Y. Tang, "Pulse density modulation for maximum efficiency point tracking of wireless power transfer systems," *IEEE Trans. Power Electron.*, vol. 33, no. 6, pp. 5492–5501, Jun. 2018.

[22] B. Nguyen *et al.*, "An efficiency optimization scheme for bidirectional inductive power transfer systems," *IEEE Trans. Power Electron.*, vol. 30, no. 11, pp. 6310–6319, Nov. 2015.

[23] Y. Jiang *et al.*, "Phase-locked loop combined with chained trigger mode used for impedance matching in wireless high power transfer," *IEEE Trans. Power Electron.*, vol. 35, no. 4, pp. 4272–4285, Apr. 2020.

[24] B. Nguyen, X. Zhang, A. Ferencz, T. Takken, R. Senger, and P. Coteus, "Analytic model for power MOSFET turn-off switching loss under the effect of significant current diversion at fast switching events," in *Proc. IEEE Appl. Power Electron. Conf.*, 2018, pp. 287–291.

[25] D. Kobayashi, T. Imura and Y. Hori, "Real-time coupling coefficient estimation and maximum efficiency control on dynamic wireless power transfer using secondary DC-DC converter," in *Proc. IEEE Ind. Electron. Soc.*, 2015, pp. 4650–4655.

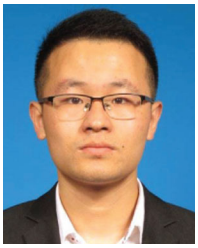

Fei Xu (Student Member, IEEE) received the B.Eng. degree from China Agricultural University, Beijing, China, in 2016, and the M.Phil. degree in electrical engineering from the Institute of Electrical Engineering, Chinese Academy of Sciences, Beijing, China, in 2019. He is currently working toward the Ph.D. degree with the Department of Electronic and Information Engineering, Hong Kong Polytechnic University, Hong Kong.

His current research interests include wireless power transfer technology and bidirectional dual-active-bridge dc–dc converters.

Siu-Chung Wong (Senior Member, IEEE) received the B.Sc. degree in physics from the University of Hong Kong, Hong Kong, in 1986, the M.Phil. degree in electronics from the Chinese University of Hong Kong, Hong Kong, in 1989, and the Ph.D. degree from the University of Southampton, Southampton, U.K., in 1997.

In 1988, he joined The Hong Kong Polytechnic University, Hong Kong, as an Assistant Lecturer. He is currently an Associate Professor with the Department of Electronic and Information Engineering, The Hong Kong Polytechnic University, where he conducts research in power electronics. From 2012 to 2015, he was a Chutian Scholar Chair Professor with the Hubei Provincial Department of Education, China, and the appointment was hosted by the Wuhan University of Science and Technology, Wuhan, China. In 2013, he was a Guest Professor with the School of Electrical Engineering, Southeast University, Nanjing, China. He was a Visiting Scholar with the Center for Power Electronics Systems, Virginia Tech, VA, USA, in November 2008, Aero-Power Sci-tech Center, Nanjing University of Aeronautics and Astronautics, Nanjing, China, in January 2009, and the School of Electrical Engineering, Southeast University, Nanjing, China, in March 2012.

Dr. Wong is a member of Electrical College, Institution of Engineers, Australia. He is an Editor for the *Energy and Power Engineering Journal* and a member of the Editorial Board of the *Journal of Electrical and Control Engineering*. He is a Guest Associate Editor for the IEEE JOURNAL OF EMERGING AND SELECTED TOPICS IN POWER ELECTRONICS, Special Issue on "Power Electronics for Biomedical Applications" in 2014 and an Associate Editor for the IEEE TRANSACTIONS ON CIRCUITS AND SYSTEMS II.

Chi K. Tse (Fellow, IEEE) received the B.Eng. (Hons.) degree with first class honors and the Ph.D. degree from the University of Melbourne, Melbourne, VIC, Australia, in 1987 and 1991, respectively, both in electrical engineering.

He is currently an Associate Vice-President (Research) and Chair Professor of electrical engineering with the City University of Hong Kong, Hong Kong. His interests include power electronics, complex networks, and disease spreading models.

Dr. Tse serves as an Editor-in-Chief for the IEEE TRANSACTIONS ON CIRCUITS AND SYSTEMS II (2016–2019), *IEEE Circuits and Systems Magazine* (2012–2015), and *IEEE Circuits and Systems Society Newsletter* (since 2007), an Associate Editor for three IEEE Journal/Transactions, Editor for *International Journal of Circuit Theory and Applications*, and is on the editorial board of the IEEE PROCEEDINGS. He was the recipient of a number of research and industry awards, including Prize Paper Awards by IEEE TRANSACTIONS ON POWER ELECTRONICS in 2001, 2015, and 2017, RISP Journal of Signal Processing Best Paper Award in 2014, Best Paper Award by International Journal of Circuit Theory and Applications in 2003, two Gold Medals at the International Inventions Exhibition in Geneva in 2009 and 2013, a Grand Prize and Gold Medal at the Silicon Valley International Invention Festival in 2019, and a number of recognitions by the academic and research communities, including honorary professorship by several Chinese and Australian universities, Chang Jiang Scholar Chair Professorship, IEEE Distinguished Lectureship, Distinguished Research Fellowship by the University of Calgary, Gledden Fellowship and International Distinguished Professorship-at-Large by the University of Western Australia.